

# A theoretical study of halo structure using elastic proton-nucleus scattering\*

CAO Dong-Liang(曹东亮)<sup>1,1)</sup> REN Zhong-Zhou(任中洲)<sup>1,2</sup> DONG Tie-Kuang(董铁矿)<sup>3</sup>

<sup>1</sup> Department of Physics, Nanjing University, Nanjing 210008, China

<sup>2</sup> Center of Theoretical Nuclear Physics, National Laboratory of Heavy-Ion Accelerator, Lanzhou 730000, China

<sup>3</sup> Macau University of Science and Technology, Macau 999078, China

**Abstract:** Elastic proton scattering from Be, C, and O isotopes has been investigated in the relativistic impulse approximation (RIA). In the calculations, the nucleon-nucleus optical potentials are obtained using ground state nuclear matter densities, which are computed using the relativistic mean field model with the FSU parameter set. The scattering observables, including differential cross section, analyzing power, and spin-rotation function, are analyzed. It is found that the scattering observables for O isotopic chains display a clear mass dependence, for instance, the minimum analyzing power shifts to a low scattering angle with increasing mass number. While for the Be isotopic chain, the emergence of a neutron halo in <sup>14</sup>Be breaks this trend, i.e., the minimum analyzing powers for <sup>12</sup>Be and <sup>14</sup>Be are almost the same as each other.

**Key words:** relativistic impulse approximation, elastic proton-nucleus scattering, neutron halo

**PACS:** 21.10.Gv, 25.40.Cm, 27.20.+n **DOI:** 10.1088/1674-1137/37/3/034103

## 1 Introduction

Elastic proton scattering has, until now, been a good method to investigate the nuclear structure of exotic nuclei. For example, the matter densities of He and Li isotopes have been measured by Egelhof et al. [1], and the halo structures of <sup>11</sup>Li and <sup>6,8</sup>He demonstrate themselves. The present paper is interested in how the existence of halo structure in a target nucleus will influence elastic proton-nucleus scattering. As is well known, relativistic impulse approximation (RIA) can describe the nucleon-nucleus (NA) scattering observables well at laboratory kinetic energies of 200 MeV and above [2, 3]. Therefore, we used the RIA model to study proton scattering. During calculations, the nucleon-nucleon (NN) amplitudes and medium modifications from Pauli blocking are treated by the relativistic Love-Franey (RLF) method, as in Refs. [4, 5]. In the RIA calculations, the ground-state matter density of the target nucleus is necessary as input, so a reliable model is needed to produce the nuclear matter density. In this paper, the Dirac-Hartree approximation with the FSU parameter set is used [6]. The introduction of  $\omega$ - $\rho$  coupling in the model will influence the neutron densities of nuclei with large

isospin asymmetry. Since the purpose of this paper is to study the observable effects of the neutron halo in elastic proton scattering, we will choose this parameter set to produce proton and neutron densities. We will choose Be, C, and O isotopes as the research objects.

This paper is outlined as follows. The RMF model with the FSU parameter set and the relativistic impulse approximation with the RLF model are described briefly in Section 2. The numerical results for p-nucleus scattering from Be, O, and C isotopes are given in Section 3, and a summary is provided in Section 4.

## 2 Theory

### 2.1 The FSU parameter set used in relativistic Hartree calculations

In the RIA model, the field felt by the projectile is described by the optical potential where the proton and neutron densities are used. In this paper, these densities will be produced by the relativistic Hartree calculations [7] with the FSU parameter set. The interacting Lagrangian density for this model is shown as follows [6]:

$$\mathcal{L}_{\text{int}} = \bar{\psi} \left[ g_S \phi - \left( g_V V_\mu + \frac{g_\rho}{2} \boldsymbol{\tau} \cdot \mathbf{b}_\mu + \frac{\epsilon(1+\tau_3)}{2} A_\mu \right) \gamma^\mu \right] \psi$$

Received 14 June 2012

\* Supported by National Natural Science Foundation of China (11035001, 11120101005, 10735010, 10975072), 973 National Major State Basic Research and Development of China (2007CB815004, 2010CB327803) CAS Knowledge Innovation Project (KJCX2-SW-N02), Research Fund of Doctoral Point (RFDLP) (20100091110028) and Project Funded by Priority Academic Programme Development of Jiangsu Higher Education Institutions (PAPD)

1) E-mail: cdl\_0102@yahoo.com.cn

©2013 Chinese Physical Society and the Institute of High Energy Physics of the Chinese Academy of Sciences and the Institute of Modern Physics of the Chinese Academy of Sciences and IOP Publishing Ltd

$$\begin{aligned}
 & -\frac{\kappa}{3!}(g_S\phi)^3 - \frac{\lambda}{4!}(g_S\phi)^4 + \frac{\zeta}{4!}g_V^4(V_\mu V^\mu)^2 \\
 & + A_V(g_\rho^2 \mathbf{b}_\mu \cdot \mathbf{b}^\mu)(g_V^2 V_\mu V^\mu). \quad (1)
 \end{aligned}$$

Here  $\phi$ ,  $V_\mu$ ,  $\mathbf{b}_\mu$  and  $A_\mu$  represent the scalar  $\sigma$  meson, vector  $\omega$  meson, isovector  $\rho$  meson, and photon, respectively.

Table 1. The FSU parameter set mentioned above.

The  $\kappa$  parameter and the meson masses ( $m_{S,V,\rho}$ ) are given in MeV, and the nucleon mass is fixed at  $M=936$  MeV.

$m_S$	$m_V$	$m_\rho$	$g_S^2$	$g_V^2$
491.500	782.500	763.000	112.1996	204.5469
$g_\rho^2$	$\kappa$	$\lambda$	$\zeta$	$A_V$
138.4701	1.4203	0.023762	0.06	0.030

In relativistic mean field theory, the Dirac equation describing the nucleon in the nucleus is deduced from the Euler-Lagrangian equation and takes the following form under mean field approximation:

$$\begin{aligned}
 & \left[ i\gamma_\mu \partial^\mu - g_V \gamma^0 V_0(r) - \frac{g_\rho \tau_3}{2} \gamma^0 \rho_0(r) - \frac{(1+\tau_3)e}{2} \gamma^0 A_0(r) \right. \\
 & \left. - M + g_S \phi_0(r) \right] \psi_i(x^\mu) = 0. \quad (2)
 \end{aligned}$$

Here  $V_0$ ,  $\rho_0$ , and  $A_0$  are the time-like components of the fields of the  $\omega$  meson,  $\rho$  meson, and photon, respectively, whose field equations can be deduced in the same way. Numerical calculations provide the ground state properties of the nucleus, such as the nuclear matter density distributions used in the later calculations:

$$\begin{aligned}
 \rho_S &= \sum_{i=1}^A \bar{\psi}_i \psi_i, \\
 \rho_V &= \sum_{i=1}^A \bar{\psi}_i \gamma^0 \psi_i. \quad (3)
 \end{aligned}$$

## 2.2 RIA calculations with the RLF model

The impulse approximation is named from the assumption, that is one can neglect the binding forces between nucleons in the target nucleus when a collision caused by an incident particle occurs. Considering some other assumptions, it will be reasonable to decompose the nucleon-nucleus scattering into a composition of nucleon-nucleon collisions, and avoid a many-body problem [8]. An optical potential, which is determined by the free NN amplitudes and target nuclear densities, is defined in RIA to describe the potential felt by the projectile during scattering. Scattering observables are then computed by solving the Dirac equation of the projectile with the optical potential introduced into it. Mc-

Neil [2] and Clark [3] et al. found good agreement between the experimental data and the results of medium energy elastic proton scattering from the RIA calculations. Considering the modifications from Pauli blocking and exchange corrections, Horowitz [4] provided an RLF model, which can deal with proton elastic scattering at a projectile energy near or above 200 MeV.

The original RIA presents the optical potential as a function of the momentum transfer  $q$  and center-of-mass energy  $E_c$  for a projectile and a target nucleon:

$$U_{\text{opt}}(q, E_c) = -\frac{4\pi ip}{M} \langle \psi | \sum_{n=1}^A e^{i\mathbf{q}\cdot\mathbf{r}(n)} \hat{F}(q, E_c; n) | \psi \rangle. \quad (4)$$

Here  $p$  is the momentum of the projectile in the nucleon-nucleus cm frame, and  $\psi$  is the ground state wave function of the target nucleus. At lower energies, the scattering operator  $\hat{F}$  is taken as a sum of five Lorentz invariants  $F^i$  ( $i=S, V, PV, T, A$ ), given by

$$\begin{aligned}
 \hat{F} &= F^S + F^V \gamma_0^\mu \gamma_{1\mu} + F^{PV} \frac{q_0^5 q_1^5}{2M 2M} + F^T \sigma_0^{\mu\nu} \sigma_{1\mu\nu} \\
 &+ F^A \gamma_0^5 \gamma_0^\mu \gamma_1^5 \gamma_{1\mu}, \quad (5)
 \end{aligned}$$

where 0 and 1 stand for the incident and struck nucleons. In the RLF model, these five invariants are written as

$$F^i(q, E_c) = i \frac{M^2}{2E_c k_c} [F_D^i(q) + F_X^i(Q)], \quad (6)$$

$$F_D^i(q) = \sum_j \delta_{i,j} (\boldsymbol{\tau}_0 \cdot \boldsymbol{\tau}_1)^{I_j} f^j(q), \quad (7)$$

$$F_X^i(q) = (-1)^T \sum_j c_{j,i} (\boldsymbol{\tau}_0 \cdot \boldsymbol{\tau}_1)^{I_j} f^j(Q), \quad (8)$$

with

$$f^i(q) = f_R^i(q) - i f_I^i(q), \quad (9)$$

$$f_R^i(q) = \frac{g_i^2}{q^2 + m_i^2} \left( 1 + \frac{q^2}{\Lambda_i^2} \right)^{-2}, \quad (10)$$

$$f_I^i(q) = \frac{\bar{g}_i^2}{q^2 + i\bar{m}_i^2} \left( 1 + \frac{q^2}{\Lambda_i^2} \right)^{-2}, \quad (11)$$

where  $c_{j,i}$  is the element of the Fierz matrix (seen in Ref. [4] or [5]) and  $T$  is the isospin of the two-nucleon state. For the pp and pn scattering, these invariants can be, respectively, taken as

$$F^i(pp) = F^i(T=1), \quad (12a)$$

$$F^i(pn) = \frac{1}{2} [F^i(T=1) + F^i(T=0)]. \quad (12b)$$

For a spin-saturated nucleus, considering parity, the optical potential in Eq. (4) takes the form of Eq. (14),

and is separated into direct and exchange contributions:

$$U_{\text{opt}}(q) = -\frac{4\pi ip}{M}[F^{\text{S}}(q)\rho_{\text{S}}(q)+\gamma^0 F^{\text{V}}(q)\rho_{\text{V}}(q)] \quad (13)$$

$$= U^{\text{S}}+\gamma^0 U^{\text{V}}, \quad (14)$$

where

$$U^i=U_{\text{D}}^i+U_{\text{X}}^i, \quad i=\text{S},\text{V}. \quad (15)$$

After taking Fourier transforms, the direct and exchange terms of  $U_{\text{opt}}(r, E)$  are shown as:

$$U_{\text{D}}^i(r, E) = -\frac{4\pi ip}{M} \int d^3x' \rho^i(\mathbf{x}') t_{\text{D}}^i(|\mathbf{x}'-\mathbf{x}|; E), \quad (16)$$

$$U_{\text{X}}^i(r, E) = -\frac{4\pi ip}{M} \int d^3x' \rho^i(\mathbf{x}', \mathbf{x}) t_{\text{X}}^i(|\mathbf{x}'-\mathbf{x}|; E) \quad (17)$$

$$j_0(p|\mathbf{x}'-\mathbf{x}|), \quad (18)$$

where

$$t^i(|\mathbf{x}|, E) = \int \frac{d^3q}{(2\pi)^3} t^i(q, E) e^{-i\mathbf{q}\cdot\mathbf{x}}, \quad (19)$$

with  $t^i(q, E) = (iM^2/2Ek)F^i(q)$ . The nuclear densities are defined as:

$$\rho^i(\mathbf{x}', \mathbf{x}) = \sum_{n=1}^A \bar{\psi}_n(\mathbf{x}') \lambda^i \psi_n(\mathbf{x}), \quad (20a)$$

$$\rho^i(\mathbf{x}) = \rho^i(\mathbf{x}, \mathbf{x}). \quad (20b)$$

We found that the free NN scattering amplitudes and the nuclear matter density distributions of the target nucleus are the essential ingredients used to generate the optical potential. The experimental data on proton elastic scattering can also prompt a phenomenological optical potential, which can be taken as a reference. The original RIA approximates the scattering between the projectile and target nucleon as free NN scattering. While this approximation is valid at high energies, it is necessary to correct the optical potential for medium modifications from Pauli blocking as follows:

$$U^i(r, E) \rightarrow \left[ 1 - a(E) \left( \frac{\rho_{\text{B}}(r)}{\rho_0} \right)^{2/3} \right] U^i(r, E), \quad (21)$$

with  $\rho_0 = 0.1934 \text{ fm}^{-3}$ . Then the optical potential is applied into the Dirac equation for the projectile, as shown in Eq. (22):

$$\begin{aligned} & -i\boldsymbol{\alpha}\cdot\nabla+U^{\text{V}}(r, E)+\beta[M+U^{\text{S}}(r, E)]\mathcal{U}(r, E) \\ & = EU(r, E). \end{aligned} \quad (22)$$

After some algebra, the Dirac equation becomes

$$\begin{aligned} & (-\nabla^2+V_{\text{cent}}+V_{\text{so}}\boldsymbol{\sigma}\cdot\mathbf{L}+V_{\text{Darwin}})u(\mathbf{x}) \\ & = (E^2-M^2)u(\mathbf{x}). \end{aligned} \quad (23)$$

Here the optical potential is transformed into sets of

$$V_{\text{cent}} = 2MU^{\text{S}}+2EU^{\text{V}}+(U^{\text{S}})^2-(U^{\text{V}})^2, \quad (24)$$

$$V_{\text{so}} = -\frac{1}{r} \frac{A'}{A}, \quad (25)$$

$$V_{\text{Darwin}} = \frac{3}{4} \left( \frac{A'}{A} \right)^2 - \frac{1}{r} \frac{A'}{A} - \frac{1}{2} \frac{A''}{A}, \quad (26)$$

with  $A = E + M + U^{\text{S}} - U^{\text{V}}$ . The scattering amplitudes  $f(\theta)$  can be given by resolving Eq. (23):

$$f(\theta) = g(\theta) + h(\theta) \boldsymbol{\sigma} \cdot \hat{n}, \quad (27)$$

and then scattering observables, including the differential cross section ( $d\sigma/d\Omega$ ), the analyzing power ( $A_y$ ), and the spin-rotation function ( $Q$ ), are easily determined as:

$$\frac{d\sigma}{d\Omega} = |g|^2 + |h|^2, \quad (28a)$$

$$A_y = 2 \text{Re}(g^*h) / (|g|^2 + |h|^2), \quad (28b)$$

$$Q = 2 \text{Im}(gh^*) / (|g|^2 + |h|^2). \quad (28c)$$

Further details about the RIA calculations and RLF model can be found in Refs. [4, 5, 9], and the references cited therein.

## 3 Results

### 3.1 The properties of the nucleus

The results from the calculations and some available experimental data are presented in Table 2. We found that, except for the binding energy per nucleon of  $^{12}\text{C}$ , all the binding energies are in the range of permitted errors, which suggests that the FSU parameter set is still credible for the computation of nuclei in the light nuclear area, especially for neutron-rich nuclei. Compared with the homogeneous tiny variation in the neutron skin of the O isotopes,  $^{14}\text{Be}$  and  $^{16}\text{C}$  have noticeable differences between the proton and neutron rms radii, especially  $^{14}\text{Be}$ .

The neutron density distributions ( $\rho_{\text{V}}$ ) for the O and Be isotopic chains are provided in Figs. 1 and 2, respectively. The neutron  $\rho_{\text{V}}$  of the O isotopes display good mass dependence when  $r > 2 \text{ fm}$ . As for the central part ( $r < 1 \text{ fm}$ ), if we leave  $^{14}\text{O}$  (which is a little bothersome) aside temporarily, O isotopes can be divided into two groups: the one including nuclei from  $^{16}\text{O}$  to  $^{22}\text{O}$ , and the other from  $^{24}\text{O}$  to  $^{28}\text{O}$ . Each nucleus in the first group shows a central depression of neutron  $\rho_{\text{V}}$ , while for each nucleus in the other group, the depression disappears. Things are quite different for the Be isotopic chain. There is no obvious mass dependence, which is shown in Fig. 1. The central neutron density decreases

from  $^{10}\text{Be}$  to  $^{12}\text{Be}$ , then increases from  $^{12}\text{Be}$  to  $^{14}\text{Be}$ . For  $^{14}\text{Be}$ , a long neutron tail appears, which indicates the emergence of a halo structure, as shown in Table 2.

Table 2. The rms proton radii, neutron skin, charge radii (all in fm), and binding energy per nucleon (MeV) from the relativistic Hartree calculations for the Be, C, and O isotopes. Some available experimental data [10–12] are also given.

nuclei		$R_p$	$R_n - R_p$	$R_c$	$B$
$^{10}\text{Be}$	Theo.	2.2432	0.2367	2.3854	6.2567
	Expt.	—	—	—	6.4976
$^{12}\text{Be}$	Theo.	2.2918	0.4682	2.4311	5.8368
	Expt.	—	—	—	5.7208
$^{14}\text{Be}$	Theo.	2.3027	2.1141	2.4414	4.9770
	Expt.	—	—	—	4.994
$^{12}\text{C}$	Theo.	2.3651	-0.0261	2.5004	7.1328
	Expt.	—	—	2.4703	7.6801
$^{14}\text{C}$	Theo.	2.3935	0.1603	2.5273	7.4323
	Expt.	—	—	2.5037	7.5203
$^{16}\text{C}$	Theo.	2.4206	0.6486	2.5529	6.8740
	Expt.	—	—	—	6.9221
$^{14}\text{O}$	Theo.	2.6054	-0.2259	2.7287	6.9395
	Expt.	—	—	—	7.0523
$^{16}\text{O}$	Theo.	2.5646	-0.0287	2.6899	7.9652
	Expt.	—	—	2.7013	7.9292
$^{18}\text{O}$	Theo.	2.5694	0.2312	2.6944	7.8210
	Expt.	—	—	2.7745	7.7670
$^{20}\text{O}$	Theo.	2.5777	0.3819	2.7023	7.5459
	Expt.	—	—	—	7.5686
$^{22}\text{O}$	Theo.	2.5975	0.5403	2.7213	7.2741
	Expt.	—	—	—	7.3648
$^{24}\text{O}$	Theo.	2.6265	0.6687	2.7490	6.9444
	Expt.	—	—	—	7.016
$^{26}\text{O}$	Theo.	2.6733	0.7631	2.7936	6.5261
	Expt.	—	—	—	6.457
$^{28}\text{O}$	Theo.	2.7212	0.8038	2.8396	6.0813
	Expt.	—	—	—	5.925

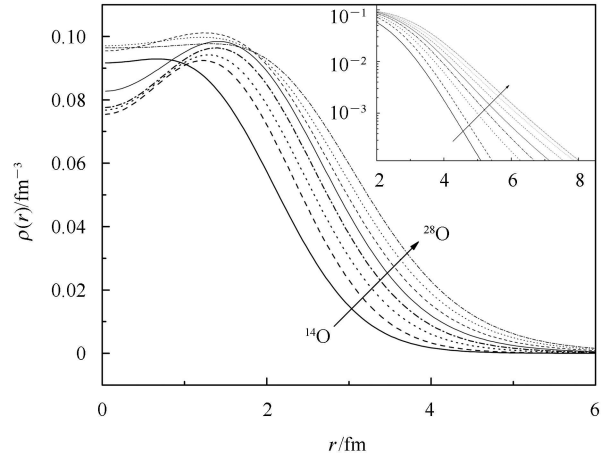


Fig. 1. Neutron density distributions ( $\rho_n$ ) for O isotopes from  $^{14}\text{O}$  to  $^{28}\text{O}$ . The inset shows the exponential neutron densities.

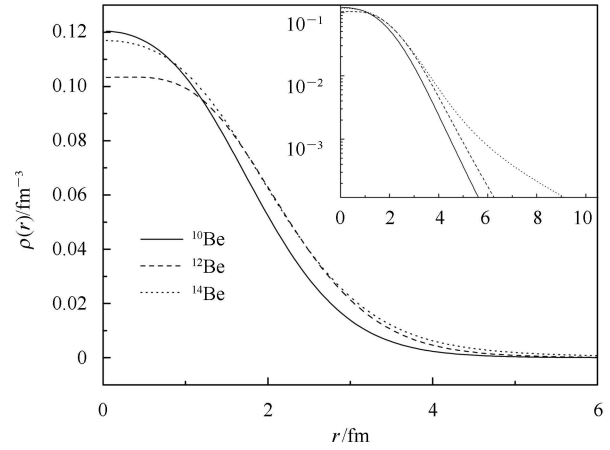


Fig. 2. The same as Fig. 1, but for Be isotopes from  $^{10}\text{Be}$  to  $^{14}\text{Be}$ .

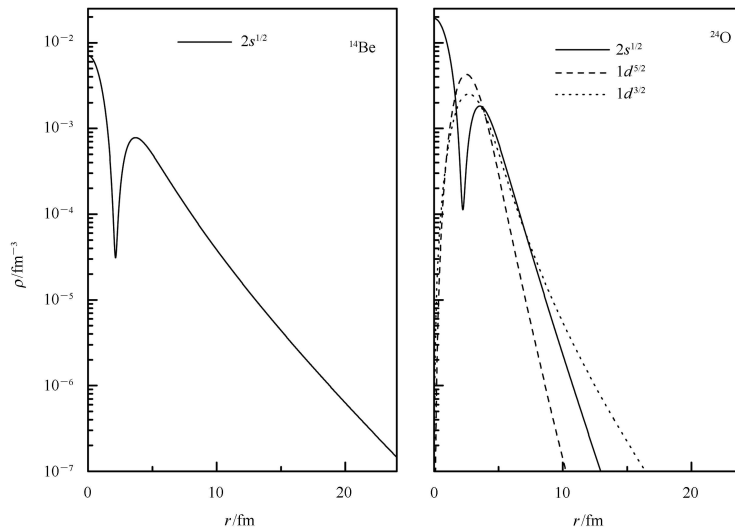


Fig. 3. The vector density distribution  $\rho_v$  of the  $2s_{1/2}$  neutron state of  $^{14}\text{Be}$ , the  $\rho_v$  of  $2s_{1/2}$ ,  $1d_{5/2}$ , and the  $1d_{3/2}$  states of  $^{24}\text{O}$ . The scalar densities  $\rho_s$  not shown here are very similar to  $\rho_v$ .

Interpretations can be found from Fig. 3. The calculation for  $^{24}\text{O}$  shows that the  $1d_{5/2}$  and  $1d_{3/2}$  neutron states have sharp peaks near  $r = 3$  fm and contribute little to the central neutron density  $\rho_V$ , while the  $2s_{1/2}$  state has a sharp central peak. For the O isotopic chain, these three neutron states are empty at  $A=16$ , then they are occupied by neutrons with increasing mass number. Since the energy of the  $1d_{5/2}$  state is the lowest and that of  $1d_{3/2}$  is the highest among the three states, neutrons will be filled first in the  $1d_{5/2}$  state, while the  $2s_{1/2}$  state is occupied simultaneously but slowly, until the  $1d_{5/2}$  state is almost fully occupied at  $A=20$ . Then the  $2s_{1/2}$  state has the priority to be occupied, which causes the rise of the central neutron density from  $^{20}\text{O}$  to  $^{24}\text{O}$ .

As for the Be isotopes, newly added neutrons are filled in a different order because of the energy level inversion between the  $1d_{5/2}$  and  $2s_{1/2}$  states. The energy of the  $2s_{1/2}$  state becomes much lower than that of the  $1d_{5/2}$  state, while the energies of the two  $1d$  states are almost the same. So the newly added neutrons will be filled first in the  $2s_{1/2}$  rather than  $1d_{5/2}$  state, causing the increase in central neutron density. Another difference is that the  $2s_{1/2}$  state of  $^{14}\text{Be}$  is depressed and has a large spatial extension, which results in the emergence of a neutron halo structure in  $^{14}\text{Be}$ . This is also due to the energy level inversion between the two states. A similar inversion happens in the C isotopic chain, while the two  $1d$  states have obvious energy difference.

### 3.2 Microscopic and phenomenological optical potential

Figure 4 shows our relativistic microscopic optical

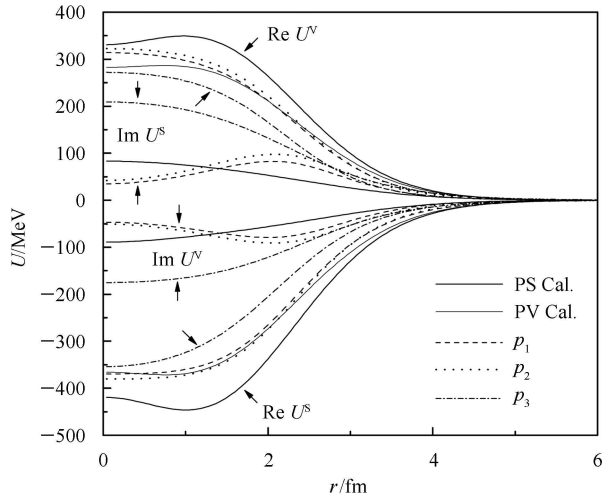


Fig. 4. Relativistic optical potentials for  $^{16}\text{O}$  at 200 MeV. The wide and narrow solid curves are the microscopic calculations with PS and PV coupling, respectively. (The imaginary parts of the two microscopic potentials are the same.) The dashed, dotted, and dash-dotted curves are the three phenomenological fits of Kobos et al. [13].

potentials for  $p+^{16}\text{O}$  elastic scattering at 200 MeV, and the phenomenological ones fit to the scattering data with the parameters given by Kobos et al. [13]. Here the microscopic optical potential using an initial pseudoscalar (PS) coupling for the “pion” piece of the scattering operator  $\hat{F}$ , which is replaced by pseudovector (PV) coupling at a lower energy in the RLF model, is also given as a reference by a wide curve, while the PV one is given by a narrow curve. We find good agreement between the PV potential and the phenomenological potentials 1 and 2, especially the real parts, while the PS potential does not agree well with the phenomenological potentials. This confirms that the RIA calculations with the RLF model are reliable in the light nuclear area.

### 3.3 Spin-orbit potential

Figure 5 presents the volume integral per nucleon of the real part of  $V_{so}$  at a 200 MeV p-nucleus scattering energy. An obvious mass dependence is shown in this figure, which can be taken as another verification of the credibility of the relativistic Hartree calculations. Figs. 6 and 7 present the real  $V_{so}$  at 200 MeV for the Be, C, and O isotopic and isotonic chains, respectively, and a clear mass dependence can also be found in Fig. 7 and the O isotopic chain in Fig. 6, except for the central part of  $V_{so}$ . Considering the spin-rotation potential of the O isotopic chain, the O isotopes can also be divided into two groups. Let us look at Eqs. (14) and (25) to give an explanation. The spin-rotation potential is a function of scalar density  $\rho_S$  and vector density  $\rho_V$ , and their first derivatives, which are the main factors influencing  $V_{so}$  because of the large magnitude of  $(E+M)$  appearing in the denominator of Eq. (25). It can be found in Fig. 3 that, for the  $1d_{5/2}$  and  $2s_{1/2}$  states of  $^{24}\text{O}$ , the first derivatives of  $\rho_V$  (and  $\rho_S$ , which are not shown in this paper for simplicity)

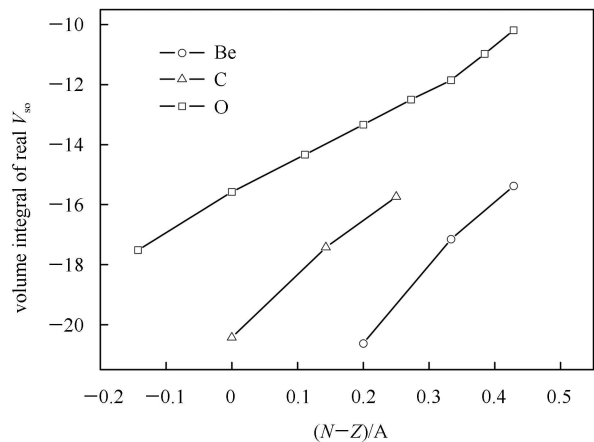


Fig. 5. The volume integral per nucleon of the real spin-orbit potentials  $V_{so}$  for the Be, C, and O isotopic chains, respectively, at a 200 MeV p-nucleus scattering energy.

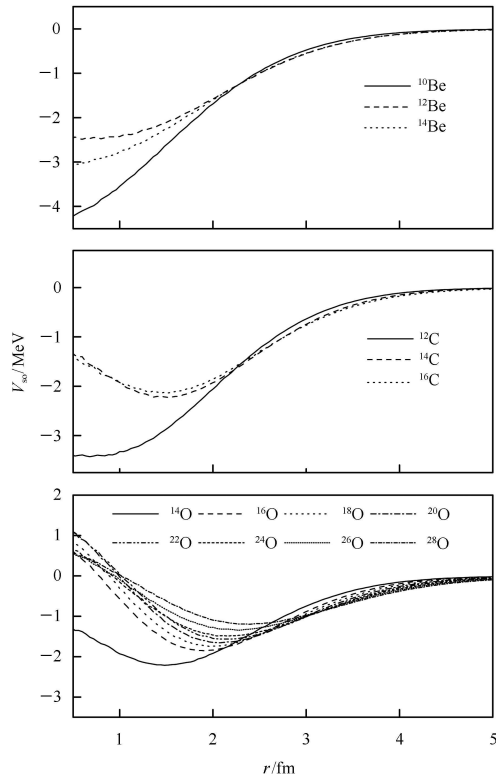


Fig. 6. The real part of the spin-orbit potentials  $V_{so}$  for the Be, C, and O isotopic chains at 200 MeV.

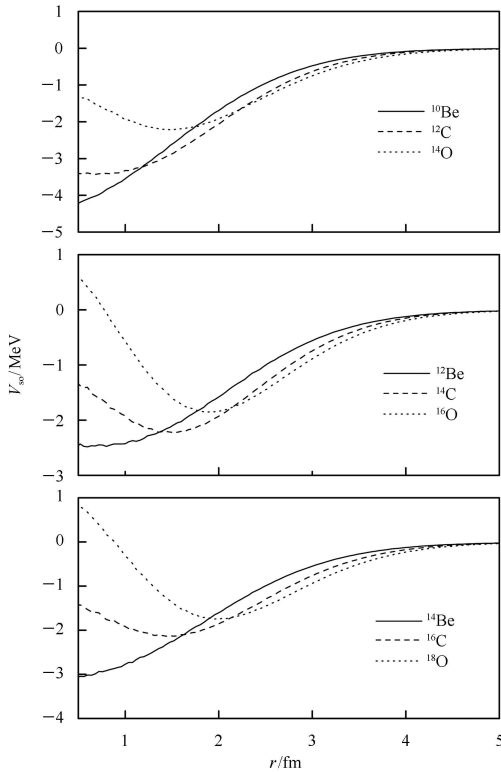


Fig. 7. The real  $V_{so}$  for the Be, C, and O isotonic chains at 200 MeV.

have the opposite sign at the central part. So, the spin-orbit potential shows a drop at  $^{24}\text{O}$ , when the  $2s_{1/2}$  state becomes preferentially occupied, which also appears at  $^{14}\text{Be}$  and  $^{16}\text{C}$ . We can find good agreement between the spin-orbit potentials and the former discussions.

### 3.4 Scattering observables

Figures 8 and 9 present the scattering observables from the RIA calculations for  $^{16}\text{O}$  and  $^{12}\text{C}$ , while the experimental data and phenomenological calculation results are given as references. We find good agreement between the better PV calculations and the experimental data in small angular regions when  $\theta < 30^\circ$ . A small difference occurs in the spin-rotation function  $Q$ , where the PS coupling calculations rather than the PV ones give better results for both  $^{16}\text{O}$  and  $^{12}\text{C}$ .

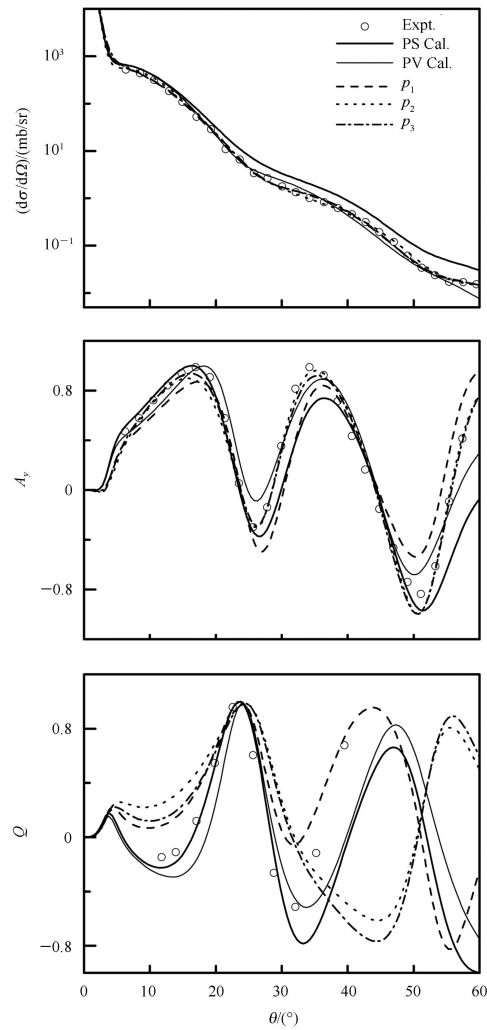


Fig. 8. The differential cross-section ( $d\sigma/d\Omega$ ), analyzing power ( $A_y$ ), and spin-rotation function ( $Q$ ) of 200 MeV proton-nucleus scattering from  $^{16}\text{O}$ . The experimental data are taken from Ref. [5]. The curves are labeled as in Fig. 4.

The proton-nucleus scattering observables for the Be, C, and O isotopes at 200 MeV are presented in Figs. 10, 11, 12, and 13. A clear mass dependence can be found in Figs. 10 and 11, as expected by analyses of

the neutron density distributions and spin-orbit potentials. Similar pictures also appear for the  $N=6,8$  isotonic chains. For the Be and C isotopic chains, as shown in Figs. 12 and 13, the mass dependence disappears because

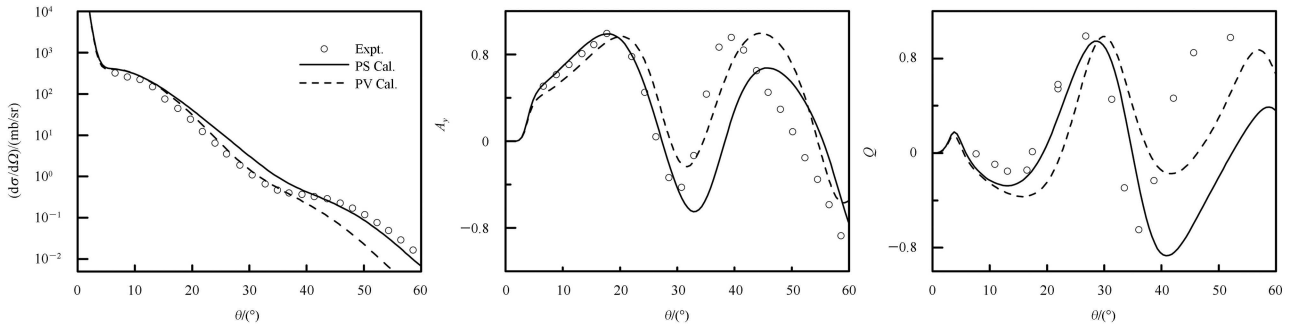


Fig. 9. The scattering observables for  $^{12}\text{C}$  at 200 MeV. The experimental data are from Ref. [5].

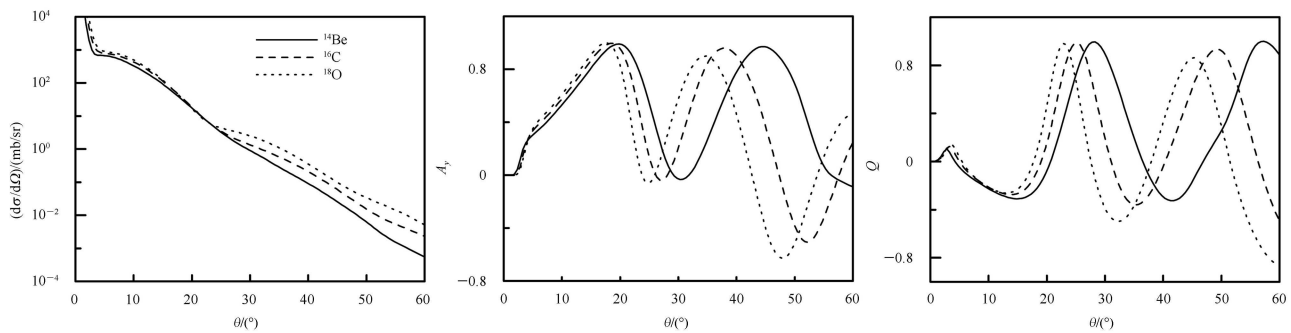


Fig. 10. The scattering observables for the  $N=10$  isotonic chain at 200 MeV.

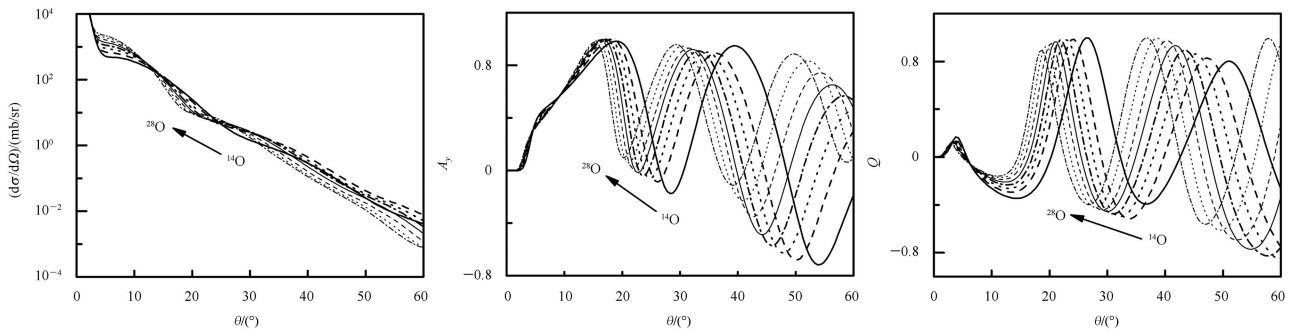


Fig. 11. The scattering observables for O isotopes at 200 MeV.

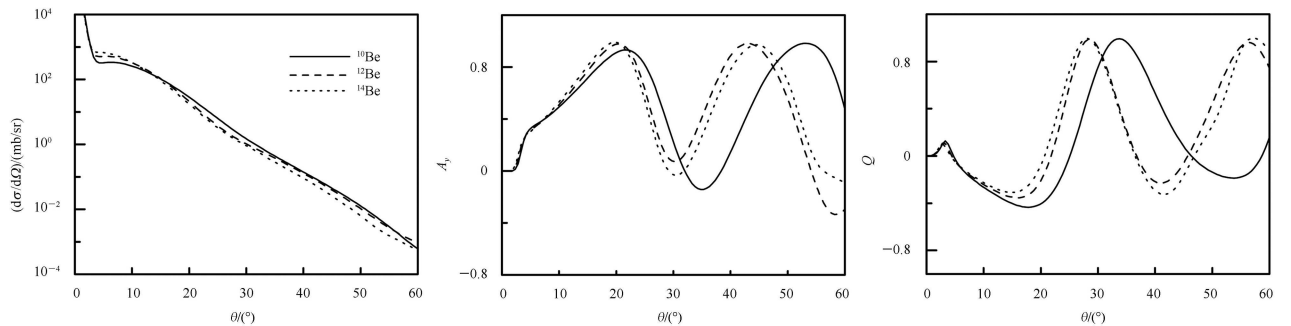


Fig. 12. The scattering observables for Be isotopes at 200 MeV.

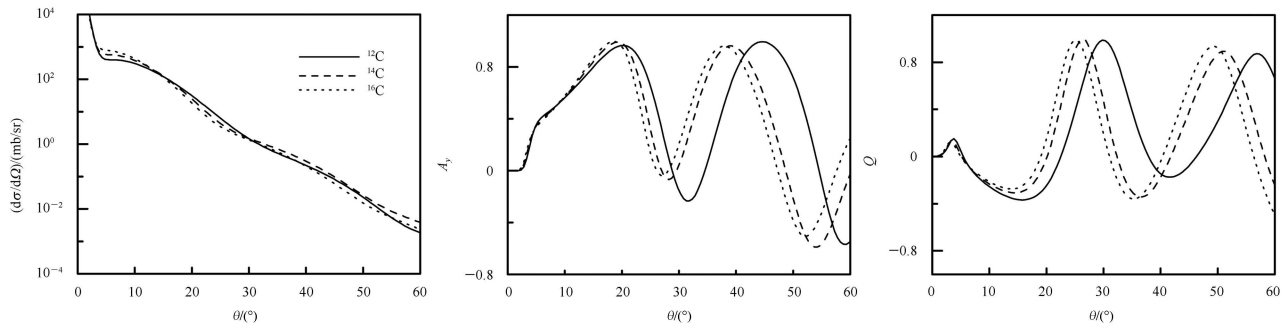


Fig. 13. The scattering observables for C isotopes at 200 MeV.

the uniform variation of ground-state properties, which is shown in the O isotopic chain, is broken in the Be and C chains by the emergence of halo structures or long neutron tails. In other words, the mass dependence shown in the O isotopic chain disappears in the Be and C chains due to the energy level inverse of the  $1d_{5/2}$  and  $2s_{1/2}$  states.

## 4 Conclusion

The ground-state properties of Be, C, and O isotopes were calculated in relativistic Hartree approximation with the FSU parameter set. For the usual isotopic chains such as O, the ground-state property changes

gradually, leading to a gradual variation in the spin-orbit potential. So the scattering observables for O isotopes present a clear mass dependence. In the Be isotopic chain, it is shown that the neutron density of the  $2s_{1/2}$  state of  $^{14}\text{Be}$  is greatly depressed, which results in a long neutron tail and a neutron halo. This is due to the energy level inversion of the  $1d_{5/2}$  and  $2s_{1/2}$  states. So in the Be isotopic chain, the uniform variation in ground-state properties and the above-mentioned mass dependence shown in the O isotopic chain are broken by the emergence of a neutron halo. In the final analysis, this can be attributed to the energy level inversion of the  $1d_{5/2}$  and  $2s_{1/2}$  neutron states of  $^{14}\text{Be}$ . A similar situation occurs in the C isotopic chain.

## References

- Egelhof P et al. Eur. Phys. J. A, 2002, **15**: 27
- McNeil J A, Shepard J R, Wallace S J. Phys. Rev. Lett., 1983, **50**: 1439; Phys. Rev. Lett., 1983, **50**: 1443
- Clark B C et al. Phys. Rev. Lett., 1983, **50**: 1644
- Horowitz C J. Phys. Rev. C, 1985, **31**: 1340
- Murdock D P, Horowitz C J. Phys. Rev. C, 1987, **35**: 1442
- Todd-Rutel B G, Piekarewicz J. Phys. Rev. Lett., 2005, **95**: 122501
- Serot D, Walecka J D. Adv. Nucl. Phys., 1986, **16**: 1
- Chew G F, Wick G C. Phys. Rev., 1952, **85**: 636
- Horowitz C J, Murdock D P, Serot B D. Computations in Nuclear Physics. Edited by Langanke K, Maruhn J A, Koonin S E. Berlin: Springer-Verlag, 1991. 129
- Angeli I. Atomic Data and Nuclear Data Tables, 2004, **87**: 185
- Audi G, Wapstra A H, Thibault C. Nucl. Phys. A, 2003, **729**: 337
- <http://www.nndc.bnl.gov/>
- Kobos A M, Cooper E D, Johansson J I. Nucl. Phys. A, 1985, **445**: 605